Thermodensity coupling in phase-field-crystal-type models for the study of rapid crystallization

Gabriel Kocher and Nikolas Provatas
Department of Physics, Centre for the Physics of Materials, McGill University, Montreal, Quebec, Canada

(Received 25 November 2018; published 14 May 2019)

We self-consistently derive a formalism that couples a phase field crystal (PFC) density field to thermal transport. It yields a theory for nonuniform transient temperature and density evolution, and includes local latent heat release during atomic rearrangements of the PFC density field. The basic formalism is applied to the original PFC model, demonstrating its capacity to capture heat transfer and recalescence in solidification. With an aim towards consistently incorporating temperature and other thermodynamic variables into PFC modeling, a new classical density field theory for solid/liquid/vapor systems is then derived. It presents a different approach to those used in the PFC literature while retaining the major advantages that have become the hallmark of PFC modeling; the new model is also based entirely on physical density, temperature, and pressure scales. We end the paper by applying the thermal-density coupling formalism to this new multiphase density functional theory/PFC model.

DOI: 10.1103/PhysRevMaterials.3.053804

I. INTRODUCTION

Solidification is a classic paradigm for understanding microstructure and phase formation in materials. The competition between thermodynamic driving forces, mass, and heat transfer and interface energy control the scale and morphology of microstructure in materials [1]. Beyond its fundamental importance to self-assembly and nonequilibrium thermodynamics, solidification is thus also of practical importance as it establishes many important properties of engineering materials [2]. Traditional theories of solidification are typically designed around the assumption that the interface is in local equilibrium, an assumption that is valid in processes operating at low solidification rates. Emerging technologies, such as those using local laser welding to additively assemble components, typically operate at rapid solidification rates [3,4]. Here, the cooling rates involved can be so large that the notion of interface equilibrium is no longer valid. This leads to the production of metastable solidified states due to solute and density trapping, and kinetic-limited morphologies that are very different from the standard dendritic forms in slow-cooling processes. Moreover, thermally induced stresses can lead to exotic atomic-scale effects such as defect migration, void formation, and precipitation of second phases near stressed interfaces [2,5,6].

Modelling the wide scope of phenomena involved in rapid solidification self-consistently is challenging due to the multiple length and time scales involved. Molecular dynamics is typically limited to times scales that preclude processes active on diffusional time scales, and in systems covering several microns. On the other end of the spectrum, traditional phase field (PF) models can capture diffusional time scales over many hundreds of microns. Their use in quantitative modeling of solidification microstructure is well documented in the literature, where matched asymptotic analysis is used to map PF models onto quantitative sharp interface theories that are quantified by a few *a priori* known microscopic parameters [7–9]. However, traditional PF theories lack an atomic-scale structure, thus precluding an explicit connection to polycrystalline solidification, grain boundary energy, interface anisotropy, void formation, and vacancy trapping, among others. Also, adding elasticity and defect flow is challenging, requiring the introduction of multiple added fields and assumed couplings between them.

Classical density functional theory (CDFT) provides an alternate route for studying crystallization and solid state transformations [10]. CDFT models are formulated in terms of a coarse grained mass density and employ multipoint correlations in the excess free energy to model interactions that govern the properties of solid phases. This makes it possible to model a wide range of metallic and nonmetallic materials. CDFT theories also naturally give rise to grain boundaries and interface kinetics arising from the atomic structure of the interface. The recent offshoot of CDFT, *phase field crystal (PFC) theory*, is a type of phase field theory with an atomic-scale order parameter related to the atomic mass density [11,12]. PFC models are rotationally invariant and do not need multiple fields to model different crystal orientations, elastic fields, or dislocations. In this paradigm grain boundaries and anisotropies are naturally captured [13–15] within the purview of a single order parameter field. These models also naturally (and with relative computational ease) give rise to a wide range of defect phenomena that are relevant to metals [16,17]. When coupled with noise, PFC models have also been used to elucidate nucleation in rapid solidification, as well as pathways for the formation of metastable phases [18–21].

An important aspect relevant to rapid solidification that has been lacking in previous PFC studies is the incorporation of thermal transport alongside the diffusive dissipative dynamics of the PFC density order parameter. At slow rates of solidification, this is a negligible effect. For example, at moderate rates of solidification relevant to laser welding of steel alloys (interface speed $v \sim 10^{-3}\,\mathrm{m/s}$ and thermal

gradient $G \sim 10^5 \mathrm{K/m}$ [22]) the thermal diffusion length ($l_T = \alpha/v \sim 1\,\mathrm{cm}$, where $\alpha \sim 1 \times 10^{-5}\,\mathrm{m^2/s}$ [23]) is much larger than the scale of microstructure ($\lambda \sim 10\,\mu\mathrm{m}$ [22]), and the thermal diffusion time ($t_D = \alpha/v^2 \sim 10\,\mathrm{s}$) is much longer than the $\sim 10^{-2}$ s solidification time of a typical 50-μm sample area. At higher solidification rates, however, thermal transport cannot be neglected. For example, at higher solidification rates used in laser welding ($v \sim 10$ m/s and $G \sim 10^6\,\mathrm{K/m}$ [22]) the thermal diffusion length ($l_T = \alpha/v \sim 1\,\mu\mathrm{m}$) is on the same order as the scale of the microstructure [22], and the thermal diffusion time $t_D \sim 10^{-7}$ s is about two orders of magnitude smaller than the $\sim 10^{-5}$ s solidification time of a 50-μm sample. Even higher solidification rates are achieved in plasma sprayed Zirconia coatings (e.g. $v \sim 1\,\mathrm{m/s}$ and $G \sim 10^8\,\mathrm{K/m}$ [24]). At the rapid solidification rates described above, thermal transport associated with latent heat of solidification is important to incorporate in a microscopic model of solidification. This is particularly crucial in determining nucleation undercooling conditions that are so critical to rapid cooling of small metal powders. It is also relevant to rapid crystallization of thin films, where it has been conjectured that the delicate balance of latent heat release and thermal dissipation drives the amorphous to crystalline transformation [25,26].

This paper derives a self-consistent formalism for coupling PFC models of a pure material to temperature transport and thermal fluctuations. We start in Sec. II by coupling the thermodynamic driving forces for mass and energy to their corresponding conservation laws, thus deriving two transport equations that couple thermal transport to microscopic mass density. This formalism is then specialized to two models in Sec. III. The first is the classical CDFT model of [10]. The second is the recent PFC model of Kocher, *et al.* [27], arriving at a model that couples the PFC order parameter to an equation for the effective PFC temperature scale. Section IV examines the properties of the latter thermal-PFC model, demonstrating thermal diffusion and latent heat release in one dimension, as well as early stage nucleation, kinetic undercooling and recalescence in rapid solidification of two-dimensional (2D) films. Section V introduces a new PFC type theory of a single component material that generalizes the work of Kocher *et al.* [27]; this decomposes the free energy into a modified Van der Waals contribution that controls the long wavelength properties of phases, and two excess contributions that, respectively, control crystallographic and other short-range properties of a crystallizing system. The aim of this model is to unify previous PFC models of solidification under a more general PFC type model that can consistently represent the properties of pure materials. Section V demonstrates the equilibrium properties of this unified model and some of its approximate forms. Section VI ends by deriving the coupling of the unified model to thermal transport by applying the formalism of Sec. III.

II. THERMODYNAMIC FLUXES AND CONSERVATION LAWS

Most formalisms of nonequilibrium thermodynamics start by relating changes in entropy to the fundamental thermodynamic fields of an evolving system. One manifestation is

$$ds = \frac{1}{T}de - \frac{\mu}{T}d\rho, \tag{1}$$

where s is the entropy density of a volume element, T is temperature, e is the internal energy density, ρ is the local average mass density, and μ is a chemical potential. Equation (1) can be taken to imply, in the mean field sense, that a volume element in a system is in local equilibrium, although it can vary from volume to volume such as to allow spatial variations of the relevant fields. We perform a functional generalization of Eq. (1) to model the spatial variation of the fields, giving

$$\delta S[e,\rho] = \int_V d\vec{x}^3 \frac{1}{T(x,t)}\,\delta e + \int_V d\vec{x}^3 \frac{1}{T(x,t)}\frac{\delta F[T,\rho]}{\delta\rho}\delta\rho, \tag{2}$$

where $F[T,\rho]$ is the free energy of the system, which depends on the temperature (T), density (ρ), and their gradients. As conserved fields, internal energy and density satisfy the conservation laws

$$\begin{aligned}\frac{\partial e}{\partial t} &= -\nabla\cdot\vec{J}_e\left(\frac{\delta S}{\delta e},\frac{\delta S}{\delta\rho}\right),\\ \frac{\partial \rho}{\partial t} &= -\nabla\cdot\vec{J}_\rho\left(\frac{\delta S}{\delta e},\frac{\delta S}{\delta\rho}\right),\end{aligned} \tag{3}$$

where $\vec{J}_e$ and $\vec{J}_\rho$ are, respectively, the energy and density fluxes. We postulate that these are linear functions of the thermodynamic driving forces, $\nabla[1/T(x,t)]$ and $\nabla[1/T(x,t)\cdot\delta F[T,\rho]/\delta\rho]$. We aim to derive a self-consistent form of this theory using experiments and symmetry to guide us where appropriate.

As a minimal description, we start by assuming that the cross effects in mass and energy diffusion can be neglected. We also choose the phenomenological Onsager coefficient for energy diffusion as $L_{uu} = KT^2/2$, where K is the thermal conductivity. This form is chosen to recover Fick's law,

$$J_e = \frac{1}{2}KT^2\nabla\frac{1}{T} = -K\nabla T. \tag{4}$$

Writing the Onsager coefficient for density diffusion as $\Gamma\rho$, where Γ may depend on temperature, gives the classic CDFT density flux for J_ρ. Combining these fluxes we can now write two conservation equations [Eqs. (3)] for energy and mass transport as

$$\begin{aligned}\frac{\partial e}{\partial t} &= K\nabla^2 T,\\ \frac{\partial \rho}{\partial t} &= \nabla\left(\Gamma(T)\rho\nabla\left(\frac{1}{T}\frac{\delta F}{\delta\rho}\right)\right).\end{aligned} \tag{5}$$

To arrive at a closed form model with thermal coupling, we must specify the free energy and its temperature and density dependencies. The details of this process for the PFC model are reserved for the next section. Here, we just mention that in general an expression for the energy density e can be derived from the free energy density by using the functional generalization of $s = -df/dT|_\rho$ that allows for gradient dependence

in the free energy density, i.e.,

$$e = f(T, \rho, \nabla\rho) - T\frac{\delta F[T, \rho, \nabla\rho]}{\delta T}. \quad (6)$$

Note that the density equation in Eq. (5) is analogous to the one used in density functional theory (DFT). In its original derivation [28], ρ was interpreted as an ensemble averaged quantity, which is why formally no noise is added to this equation. When applied to PFC modeling (or phase field modeling), noise will be added to account for stochastic events like nucleation and interface fluctuations.

III. TEMPERATURE COUPLING FOR THE BASIC CDFT AND PFC MODELS

This section specializes the formalism of the last section first to the classical CDFT model of [10], and then to the PFC model of Kocher *et al.* [27].

A. Application to CDFT theory of freezing

We consider the general free energy functional of a simple CDFT type theory of the form

$$F = \int d\mathbf{x}\, f = \int d\mathbf{x}\, k_B T\left\{\rho \ln\frac{\rho}{\bar{\rho}} - \delta\rho - \frac{1}{2}\int d\mathbf{x}'\delta\rho(\mathbf{x}')C_2\delta\rho(\mathbf{x})\right\}, \quad (7)$$

where C_2 is the two point density-density correlation function of the theory. It is nominally taken at the reference density $\bar{\rho}$ of the liquid at coexistence, but we tacitly assume that the correlation function has some T dependence away from the reference. The free energy density f varies on the length scale of the density ρ. Temperature, however, varies much more slowly than density. As a result, a sensible energy conservation equation of the form appearing in Eq. (5) should consider e coarse grained on the same length scale as the variation in the temperature. This is done by applying a smoothing operator χ on the microscopic internal energy e, or any quantity that involves the microscopic free energy functional f.

With the above considerations, we begin by computing the right-hand side of Eq. (6) using Eq. (7), which gives,

$$\frac{\partial F}{\partial T} = f/T + \int dx'\left[-\frac{1}{2}k_B T\delta\rho(x)C_2'(x, x', T)\delta\rho(x')\right], \quad (8)$$

where the notation $()' = \partial()/\partial T$ is introduced for functions of T. Substituting Eq. (8) into Eq. (6) and coarse graining gives

$$e = \chi * \left[f - T\frac{\delta F}{\delta T}\right] = \frac{1}{2}k_B T^2 \chi * \left[\int dx'[\delta\rho(x)C_2'(x, x', T)\delta\rho(x')]\right], \quad (9)$$

where $*$ denotes the convolution operation with the smoothing function χ. Equation (9) is a suitable form for internal energy to use in Eq. (5). Note that we have pulled the smoothing operation through the field T because we assume temperature is a smooth variable on the scale of atomic variations inherent in the PFC density ρ. The time derivative of Eq. (9) gives

$$\dot{e} = k_B\dot{T}\chi * \left[\int dx'\delta\rho(x)\left(TC_2' + \frac{1}{2}T^2C_2''\right)\delta\rho(x')\right] + k_B T\chi * \left[\int dx'\delta\dot{\rho}(x)TC_2'\delta\rho(x')\right], \quad (10)$$

substituting Eq. (10) into the first of Eq. (5) gives a heat equation for the general CDFT model,

$$\chi * \left[\int dx'\delta\rho(x)\left(TC_2' + \frac{1}{2}T^2C_2''\right)\delta\rho(x')\right]\frac{\partial T}{\partial t} = \frac{K}{k_B}\nabla^2 T - \chi * \left[\int dx'\delta\dot{\rho}(x)TC_2'\delta\rho(x')\right]T.$$

B. Specialization to the vapor-PFC model

We next proceed to specialize the above general PFC temperature equation to the recent vapor PFC model derived in [27]. The vapor PFC model was illustrated using the same two point correlation of the original PFC model,

$$\bar{\rho}C_2(\mathbf{x}, \mathbf{x}', T) = \left[1 - r - B_x\left(1 + R^2\nabla_x^2\right)^2\right]\delta(\mathbf{x} - \mathbf{x}'), \quad (11)$$

where R tunes the lattice constant of the PFC solid phase and ∇_x refers to differentiation with respect to dimensional variables. Here, B_x and r are dimensionless constants. The parameter r is the effective temperature parameter of the original PFC model [29]. The addition of the new third and fourth order low-k mode correlation terms introduced in [27] yields the following free energy functional:

$$F = \int d\mathbf{x}\, k_B T\bar{\rho}\left\{n\left(r + B_x\left(1 + R^2\nabla_x^2\right)^2\right)\frac{n}{2} - \frac{n^3}{6} + \frac{n^4}{12} + \left(a\frac{\bar{n}^2}{3} + b\frac{\bar{n}^3}{4}\right)n\right\}, \quad (12)$$

where a and b are constants, and where we have transformed to the dimensionless density $n(\mathbf{x}, t) = (\rho(\mathbf{x}, t) - \bar{\rho})/\bar{\rho}$, while

$$\bar{n} = \chi * n \equiv \int d\mathbf{x}'\chi(\mathbf{x} - \mathbf{x}')n(\mathbf{x}). \quad (13)$$

It is noted that in this minimal model the effective 3- and 4-point terms do not depend on temperature. This form will serve to illustrate most of the physical features of density-temperature coupling, although it is not as robust as if were to assume that these terms also depend on the temperature (more on this in Sec. V). In this derivation of a heat equation coupled to the PFC equation, we assume that only the PFC temperature scale r depends on physical temperature. One may additionally assume a temperature dependence for R, but we neglect this effect here.

To proceed with the first of Eq. (5), we start by scaling the right-hand side. We first assume a mapping from T to r of the form $T(\mathbf{x}, t) = T_0\theta(r(\mathbf{x}, t))$, where T_0 is a reference temperature, and where the dependency on $\mathbf{x}$ is written here to emphasize the spatial variation of r. It is noted that like T, the PFC temperature r is smooth at the atomic scale. This gives

$$K\nabla^2 T = KT_0\nabla_x^2\theta(r) = \frac{KT_0}{R^2}\nabla^2\theta(r), \quad (14)$$

where the last expression in Eq. (14) assumes length is rescaled according to $\mathbf{r} = \mathbf{x}/R$, and ∇ denotes dimensionless derivatives with respect to $\mathbf{r}$ (not to be confused with r). Using the chain rule gives

$$\nabla^2\theta(r) = \nabla\cdot(\nabla\theta(r)) = \nabla\cdot(\theta'\cdot\nabla r) = \theta'\nabla^2 r + \nabla\theta'\cdot\nabla r, \tag{15}$$

where θ' denoted differentiation with r. Substituting these gradients back into the internal energy equation of Eq. (5) gives

$$\begin{aligned}\frac{\dot{e}}{\bar{\rho}k_BT_0} &= \frac{K}{\bar{\rho}R^2k_B}(\theta'\nabla^2 r + \nabla\theta'\cdot\nabla r)\\ &= \mathcal{C}^*(\theta'\nabla^2 r + \nabla\theta'\cdot\nabla r),\end{aligned} \tag{16}$$

where $C^* = K/(\bar{\rho}R^2k_B)$ has units of s^{-1}. Next, we coarse grain the local internal energy density, taking Eq. (12) as input, i.e.,

$$\begin{aligned}e &= \chi*\left(f - T\frac{\delta F}{\delta T(\vec{x},t)}\right)\\ &= -\chi*\left(\frac{\bar{\rho}k_BT^2\,r'}{2}n^2\right).\end{aligned} \tag{17}$$

This leads to

$$e/\left(\bar{\rho}k_BT_0^2\right) = -\chi*\{\theta(r)^2r'n^2/2\}. \tag{18}$$

A formal expression for r' can be found by differentiating

$$\frac{\partial}{\partial T}T = T_0\frac{\partial}{\partial T}\theta(r(T)) = T_0\frac{\partial\theta}{\partial r}\frac{\partial r}{\partial T} = T_0\theta'r' = 1, \tag{19}$$

giving

$$r' = \frac{1}{T_0\theta'}. \tag{20}$$

Thus, Eq. (18) becomes

$$e/(\bar{\rho}k_BT_0) = -\theta^2/\theta'\chi*\{n^2/2\}, \tag{21}$$

where functions of $\theta(r)$ were taken out of the smoothing operations as they vary on long wavelengths by hypothesis. Taking the time derivative of Eq. (21) gives

$$\begin{aligned}\dot{e}/(\bar{\rho}k_BT_0) = &\frac{(\theta^2\theta'' - 2\theta\theta'^2)}{2\theta'^2}\chi*[n^2/2]\frac{\partial r}{\partial t}\\ &-\theta^2/\theta'\frac{\partial}{\partial t}\{\chi*[n^2/2]\}.\end{aligned} \tag{22}$$

Equating the right-hand sides of Eqs. (22) and (16) finally gives

$$\begin{aligned}\frac{(\theta^2\theta'' - 2\theta\theta'^2)}{2\theta'^2}\chi*[n^2/2]\frac{\partial r}{\partial t} &= \mathcal{C}^*(\theta'\nabla^2 r + \nabla\theta'\cdot\nabla r)\\ &+\theta^2/\theta'\frac{\partial}{\partial t}\{\chi*[n^2/2]\}.\end{aligned} \tag{23}$$

To study a minimal model of the PFC heat equation, Eq. (23), we neglect the $\nabla\theta'\cdot\nabla r$ term in Eq. (23). Also, one must determine the form of $\theta(r)$. We assume that $\theta(r)$ needs to satisfy $\theta' > 0$ (r is an increasing function of temperature) and we also assume that $F(T)$ is a concave functional of temperature $\delta^2F/\delta T^2 < 0$ for thermodynamic stability. To see the constraint that this condition sets, we calculate

$$\delta^2F/\delta T^2 = \bar{\rho}k_B\frac{n^2}{2}(2r' + Tr''). \tag{24}$$

Since $r' = 1/(T_0\theta')$ and $r'' = -1/T_0^2\theta''/\theta'^3$, the condition $\delta^2F/\delta T^2 < 0$ amounts to $(2\theta'^2 - \theta\theta'') < 0$, or just $(\theta^2\theta'' - 2\theta\theta'^2) > 0$, assuming $\theta > 0$. This is exactly the prefactor of the term on the left-hand side of Eq. (23), and confirms that the diffusion and source prefactors remain positive given the right θ function.

The lowest order $\theta(r)$ function that satisfies the two constraints is a quadratic function. For different materials, different fitting functions should be found to match T to r. To proceed here we will take the factors that involve $\theta(r)$, $\theta'(r)$ and $\theta''(r)$ in Eq. (23) as constants as we are not particularly interested in the quantitative details of how temperature affects them; varying these parameters changed results by 5–10% over the range of model temperature range simulated, and their form is only of quantitative interest once such a model is applied to a specific material. We therefore simplify Eq. (23) to a minimal heat equation for the PFC model given by

$$\chi*[n^2/2]\frac{\partial r}{\partial t} = \mathcal{C}_d\nabla^2 r + C_s\frac{\partial}{\partial t}\{\chi*[n^2/2]\}, \tag{25}$$

where $\mathcal{C}_d$ (units s^{-1}) and $\mathcal{C}_s$ (dimensionless) are parameters of the theory. It is noteworthy that Equation (25) has terms accounting for latent heat release and a susceptibility term, both directly linked to changes in the PFC density field.

IV. SIMULATIONS OF HEAT TRANSFER IN THE PFC FORMALISM

The objective of this section is to demonstrate the consistency of Eq. (25) when used with free energy F given by Eq. (12). We thus couple heat transfer to the standard PFC density dynamics [30],

$$\partial_t n(\mathbf{r}) = \Gamma\nabla^2\frac{\delta\mathcal{F}[n(\mathbf{r},t)]}{\delta n(\mathbf{r},t)} + \eta(\mathbf{r}), \tag{26}$$

where $\mathcal{F} = F/(k_BT_0\bar{\rho}R^d)$ and space has been rescaled according to $\mathbf{r} = \mathbf{x}/R$. The term $\eta(\mathbf{r})$ is a stochastic noise term used to model thermal fluctuations. It follows Gaussian statistics with its amplitude scaled by a factor N_a, and is wavelength-filtered as prescribed in [31] to assure that interface fluctuations are consistent with capillary fluctuation theory. In these units, $[\Gamma] = s^{-1}$, and so we define a characteristic time $\bar{t} = 1/\Gamma$, and scale time in our equations as $t \to t/\bar{t}$. This amounts to setting $\Gamma = 1$ in Eq. (26). Also, for simplicity, we will demonstrate the operation of Eq. (25) here for the free energy of the standard PFC model, hence setting the a, b coefficients of the vapor PFC model to zero, i.e., $a = b = c = 0$. The PFC equation Eq. (26) is coupled to the heat equation

$$\chi*[n^2/2]\frac{\partial r}{\partial t} = \mathcal{C}_d\nabla^2 r + C_s\frac{\partial}{\partial t}\{\chi*[n^2/2]\} + \mathcal{C}_b, \tag{27}$$

which is the same as Eq. (25) except with an added term $\mathcal{C}_b$ to account for heat extraction out of the simulation domain. In the remainder of this section, we promote $\mathcal{C}_d$, $\mathcal{C}_s$ and $\mathcal{C}_b$ to be simple constants of the model. We will return to the question

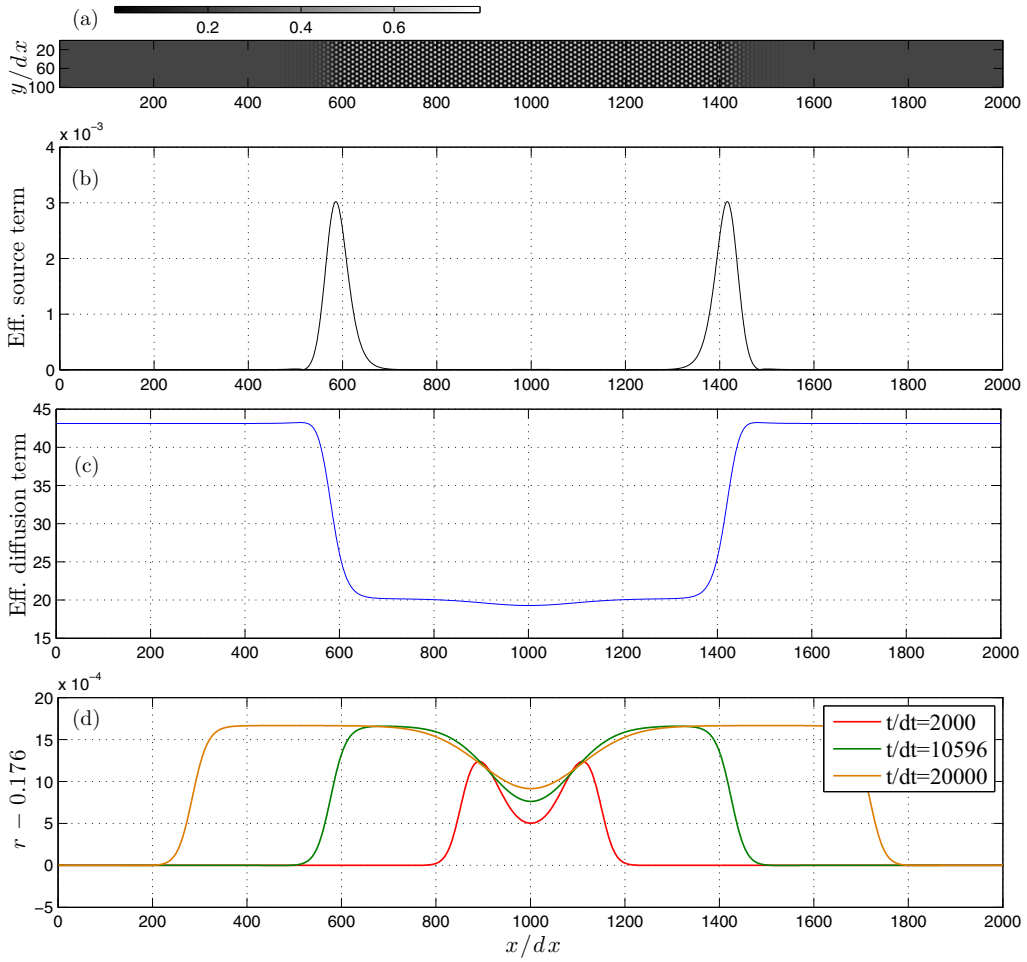

FIG. 1. Growth of a solid slab in the PFC model coupled to thermal transport. (a) shows the density field after 10 596 numerical time steps, while the other three show plots of local quantities at $y/dx = 50$ as a function of x. (b) is the effective source term $\partial_t\{\chi * [n^2/2]\}/\chi * [n^2/2]$. (c) is the effective diffusion coefficient $1/\chi * [n^2/2]$, while (d) shows the temperature field at different times. Model parameter values: $B_x = 1.5$, quench temperature $r_0 = 0.176$, average density $\langle n \rangle \equiv n_0 = 0.21$, $\mathcal{C}_s = 0.001$, $\mathcal{C}_d = 0.02$, $\mathcal{C}_b = 0$, noise amplitude $N_a = 0$, $dt = 0.25$, and $dx = 0.7256$.

of a more quantitative PFC theory, and its corresponding coupling to heat transfer int the last two sections.

We demonstrate our formalism by considering a simulation of a small 2D solidifying slab. As a first test, we consider the case where $\mathcal{C}_b = 0$ and shut off the microscopic fluctuations in the PFC density equation. A quenched liquid phase is brought in contact with a solid slab of lateral width $100dx$ (out of a total $2000dx$ in the x direction). After initial equilibration, the slab of solid grows, consuming the liquid [see Fig. 1(a)]. Due to the rearranging density, a nonzero source term is generated in the temperature equation by the term $\partial_t\{\chi * [n^2/2]\}$. This term is peaked around the regions of high density changes, i.e., the moving interface in this case. This leads to a temperature increase in and behind the interface. Some PFC temperature profiles are shown in Fig. 1(d), for early, intermediate and late time. Since $\mathcal{C}_b = 0$, the heat generated remains inside the system, and, after the interface advances through the system, the temperature reaches a plateau higher than the starting temperature of the liquid. The model's effective temperature diffusion term is scaled by $1/(\chi * [n^2/2])$, which is spatially dependent. This term is shown in Fig. 1(c), and is seen to take on very different values in the liquid and in the solid. It also reacts to smaller density and amplitude differences inside the solid phase, as seen by the slight dip in the center. Fig. 1(b) shows the last term in Eq. (27). which accounts for latent heat.

We tested the effect of nucleation on temperature in an adiabatic system. We ran a simulation of a supersaturated liquid, perturbed by density fluctuations. While the full simulation was performed in a $2000dx \times 2000dx$ box, only a small portion of this domain is shown in the insets of Fig. 2. As expected physically, several seeds eventually nucleate and grow, while releasing latent heat at interfaces. This can be seen in the insets of Fig. 2, where the thermal source term is overlaid as a color map on top of the PFC density field. This is also reflected in the main part of Fig. 2, which shows the average system temperature versus time; since the system is adiabatic, the average temperature of the system increases.

As a more stringent test of the robustness of our temperature-density PFC formulation, we proceed with a nucleation simulation in a constantly cooled system in a $2000dx \times 2000dx$ domain. A supersaturated liquid system is initialized at a high temperature (in the solid region to expedite the simulation time), and uniform heat extraction is modelled by activating the $\mathcal{C}_b$ term in Eq. (27). Density fluctuations are

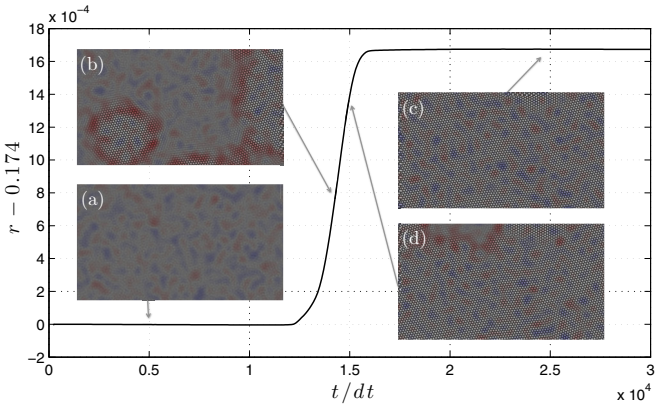

FIG. 2. The average temperature versus time, during a nucleation simulation shown in insets (a) to (d), which correspond, respectively, to 5000, 14 000, 15 000, and 25 000 dt. The density field in the insets is coloured to show the magnitude of the temperature source term, where red is a positive source term while blue is a negative source term. No colouring corresponds to nearly zero source term. Parameter values: $B_x = 1.5$, $r_0 = 0.174$, $n_0 = 0.225$, $\mathcal{C}_s = 0.001$, $\mathcal{C}_d = 0.005$, $N_a = 0.04$, $dt = 0.5$, $\lambda = 0.1$.

again incorporated. The resulting average temperature field is shown in Fig. 3, and the inset shows the corresponding density field during the nucleation process. The figure shows a strong temperature spike during nucleation, followed by a decrease in temperature as the system continues to cool.

The above simulations show the consistency of the proposed approach for coupling the PFC density order parameter to thermal transport through the PFC model's effective temperature field $r(\mathbf{x}, t)$. We have demonstrated that in the absence of noise, behavior very close to those of more traditional model C type dynamics are observed, with an effective diffusion coefficient and latent heat source that couple directly to the microscopic density field. We have also shown that the formulation is robust to density noise, making this technique useful in the study of thermal traces on microstructure

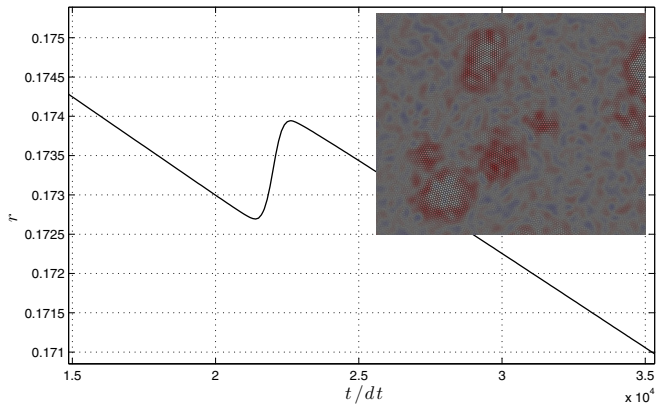

FIG. 3. Nucleation and recalescence in the thermal PFC model, with constant heat extraction of $\mathcal{C}_b = 10^{-6}$. The figure shows the average system temperature as a function of time, while the inset show a crop of the density field at $t/dt = 21661$. The color map shows the intensity of the source term in the temperature equation. Parameter values are the same as in Fig. 2.

rearrangements. One experimentally relevant example is the process of recalescence in rapidly cooled melts.

Latent heat: Mesoscopic limit of thermal PFC model

A key feature of Eq. (25) [or Eq. (23)] is that latent heat is self-consistently coupled to the PFC density. It is instructive to derive an expression for the latent heat of the thermodensity PFC model by studying its long wavelength, or phase field, limit analogously to the analyses done in [9] on *model C* [32].

We first consider a planar solidification front. We start by rewriting Eq. (25) in a one-dimensional (1D) co-moving reference frame by making the substition $\partial_t \to \partial_t - v\partial_x$, where v is the normal velocity of the front. This gives

$$\partial_t r - v\partial_x r = 2\frac{C_d\partial_x^2 r + C_s(\partial_t - v\partial_x)\chi * [n^2]}{\chi * n^2}. \tag{28}$$

Assuming a stationary situation, all explicit time varying terms can be neglected, giving

$$-v\partial_x r = 2C_d\frac{\partial_x^2 r}{\chi * n^2} - 2vC_s\frac{\partial_x(\chi * [n^2])}{\chi * n^2}. \tag{29}$$

We now consider a 1-mode approximation of the density,

$$n(\mathbf{r}) = n_0(\mathbf{r}) + \sum_{\mathbf{G}}\phi(\mathbf{r})e^{i\mathbf{G}\cdot\mathbf{r}} + \text{c.c.}, \tag{30}$$

where $n_o(\mathbf{r})$ and $\phi(\mathbf{r})$ are assumed to vary on length scales much larger than the atomic scale implied by $2\pi/|\mathbf{G}|$. Substituting this form into $\chi * n^2$ and coarse graining using standard box-averaging techniques [14] gives

$$\chi * n^2 = n_0^2 + \nu\,|\phi|^2, \tag{31}$$

where $\nu = 2$ in one dimension and $\nu = 6$ in two dimensions. Substituting the above coarse grained expression into Eq. (29) gives

$$-v\partial_x r = 2C_d\frac{\partial_x^2 r}{n_0^2 + \nu|\phi|^2} - 2vC_s\frac{\partial_x\left(n_0^2 + \nu|\phi|^2\right)}{n_0^2 + \nu|\phi|^2}. \tag{32}$$

It is reasonable to assume that the temperature field is much smoother than both the average density and the amplitude, which vary on the scale of the solid-liquid interface width 2ϵ ($\sim$ a few nm in metals). Assuming the interface is centered on 0, we integrate across the interval from $-\epsilon$ to $+\epsilon$ yielding

$$\begin{aligned}-v\int_{-\epsilon}^{+\epsilon} dx\,\partial_x r = {} & 2C_d\int_{-\epsilon}^{+\epsilon} dx\frac{\partial_x^2 r}{n_0^2 + \nu|\phi|^2} \\ & - 2vC_s\int_{-\epsilon}^{+\epsilon} dx\frac{\partial_x\left(n_0^2 + \nu|\phi|^2\right)}{n_0^2 + \nu|\phi|^2}.\end{aligned}$$

Completing the first and last integrals gives

$$\begin{aligned}v[r]_{-\epsilon}^{+\epsilon} = {} & -2C_d\int_{-\epsilon}^{+\epsilon} dx\frac{\partial_x^2 r}{n_0^2 + \nu|\phi|^2} \\ & + 2vC_s\left[\ln\left(n_0^2 + \nu|\phi|^2\right)\right]_{-\epsilon}^{+\epsilon}.\end{aligned} \tag{33}$$

In the limit of $\epsilon \to 0$, $r(\mathbf{r})$ remains a smooth function across the interface in comparison to $n_0(\mathbf{r})$ and $\phi(\mathbf{r})$, which become step functions to lowest order on the scale of variation of $r(\mathbf{r})$. Taking $-\epsilon$ to be the solid side of the interface interval and

$+\epsilon$ the liquid side, and integrating the remaining integral in Eq. (33) by parts gives,

$$\int_{-\epsilon}^{+\epsilon} dx \frac{\partial_x^2 r}{n_0^2+\nu|\phi|^2} = \frac{1}{n_l^2}\frac{\partial r}{\partial x}\bigg|_{\epsilon^+} - \frac{1}{n_s^2+\nu|\phi_s|^2}\frac{\partial r}{\partial x}\bigg|_{\epsilon^-} - \int_{-\epsilon}^{\epsilon} dx \frac{\partial}{\partial x}\left(\frac{1}{n_o^2+\nu|\phi|^2}\right)\frac{\partial r}{\partial x}, \quad (34)$$

where ϕ_s is the order parameter of the solid phase and n_s and n_l are the solid and liquid average densities, respectively. The derivative in the last integral in Eq. (34) is a sharply peaked function at the interface on the scale of the smooth function $\partial r/\partial x$. The last integral in Eq. (34) thus remains bounded and vanishes as $\epsilon \to 0$. This can also be seen by integrating the last term in Eq. (34) by parts and approximating $r \approx$ const. at $x = 0$. This makes it possible to remove r from the integral, leaving an odd function around $x = 0$, which vanishes as $\epsilon \to 0$. Substituting the result of Eq. (34) into Eq. (33) thus yields, in the limit of small ϵ,

$$0 = 2C_d\left(\frac{1}{n_s^2+\nu|\phi|^2}\frac{\partial r}{\partial x}\bigg|_{\epsilon^-} - \frac{1}{n_l^2}\frac{\partial r}{\partial x}\bigg|_{\epsilon^+}\right) - 2\nu C_s \ln\left(\frac{n_s^2+\nu|\phi_s|^2}{n_l^2}\right). \quad (35)$$

Rearranging the terms in Eq. (35) gives

$$\frac{2C_d}{n_s^2+\nu|\phi_s|^2}\frac{\partial r}{\partial x}\bigg|_{\epsilon^-} - \frac{2C_d}{n_l^2}\frac{\partial r}{\partial x}\bigg|_{\epsilon^+} = 2\nu\, C_s \ln\left(\frac{n_s^2+\nu|\phi_s|^2}{n_l^2}\right). \quad (36)$$

Equation (36) is the classic heat flux conservation across the interface. It will be shown below that the logarithmic term is proportional to the latent heat.

We can also analyze Eq. (32) by integrating both sides from $-\infty$ to $+\infty$, analogous to projection operator approaches [33]. This gives

$$-\nu\int_{-\infty}^{+\infty} dx \partial_x r = 2C_d\int_{-\infty}^{+\infty} dx \frac{\partial_x^2 r}{n_0^2+\nu|\phi|^2} - 2\nu C_s\int_{-\infty}^{+\infty} dx \frac{\partial_x\left(n_0^2+\nu|\phi|^2\right)}{n_0^2+\nu|\phi|^2}. \quad (37)$$

The middle integral in Eq. (37) is zero in the limit of $\epsilon \to 0$. This can be shown by breaking the integral into three pieces as follows,

$$\int_{-\infty}^{+\infty} dx \frac{\partial_x^2 r}{n_0^2+\nu|\phi|^2} = \int_{-\infty}^{-\epsilon} dx \frac{\partial_x^2 r}{n_0^2+\nu|\phi|^2} + \int_{+\epsilon}^{+\infty} dx \frac{\partial_x^2 r}{n_0^2+\nu|\phi|^2} + \int_{-\epsilon}^{+\epsilon} dx \frac{\partial_x^2 r}{n_0^2+\nu|\phi|^2}. \quad (38)$$

Using the approximations $n_o = n_s$ and $\phi = \phi_s$ for $x > \epsilon$ and $n_o = n_l$ and $\phi = 0$ for $x < -\epsilon$ in the first two integrals on the right-hand side of Eq. (38), and using the results of Eq. (34), gives

$$\int_{-\infty}^{+\infty} dx \frac{\partial_x^2 r}{n_0^2+\nu|\phi|^2} \approx \frac{1}{n_s^2+\nu|\phi_s|^2}\frac{\partial r}{\partial x}\bigg|_{\epsilon^-} - \frac{1}{n_l^2}\frac{\partial r}{\partial x}\bigg|_{\epsilon^+} + \int_{-\epsilon}^{+\epsilon} dx \frac{\partial_x^2 r}{n_0^2+\nu|\phi|^2} = 0 \quad (39)$$

in the limit of $\epsilon \to 0$. These considerations reduce Eq. (37) to

$$\Delta r \equiv r_s - r_L = 2C_s \ln\left(\frac{n_s^2+\nu|\phi_s|^2}{n_l^2}\right). \quad (40)$$

Equation (40) predicts a temperature rise as an undercooled liquid orders its density across the solid-liquid interface. This prediction can directly be compared to the results in Fig. 1, where we observe $\Delta r_{\text{simulation}} = 0.00166$. For the given parameters, the 1-mode approximation calculation from the phase diagram calculation predicts $\phi_s = 0.09466$. Substituting this in Eq. (40) yields $\Delta r_{\text{simulation}} = 0.00159$, which is a 4% deviation from the simulation result, in excellent agreement with the analytical derivation of Eq. (40).

The PFC temperature change Δr can be more closely related to the latent heat source term in the *Model C* phase field theory for thermally controlled solidification [32]. In the Standard Model C formulation, the starting point is the heat equation of the form

$$\dot{T} = \alpha\nabla^2 T + L\frac{h'(\phi)}{C_p}\frac{\partial\phi}{\partial t}. \quad (41)$$

We rescale this equation to PFC units with $T(r) = T_0\theta(r)$, yielding

$$\dot{r} = \alpha\nabla^2 r + \alpha\frac{\nabla\theta'\cdot\nabla r}{\theta'} + \frac{L}{T_0\theta'}\frac{h'(\phi)}{C_p}\frac{\partial\phi}{\partial t}. \quad (42)$$

Neglecting the cross terms and going through a similar procedure that leads to Eq. (32) gives,

$$\Delta r = \frac{L}{T_0\theta' C_p}. \quad (43)$$

Identifying this expression with the latent heat expression in the thermal PFC model [Eq. (40)] gives,

$$L/(T_0 C_p) = \Delta r\theta' = 2C_s\theta' \ln\left(\frac{n_s^2+\nu\phi_s|^2}{n_l^2}\right). \quad (44)$$

Note that mapping coefficients aside, this expression depends on both the average density and the amplitude. In the traditional phase field limit, there is no density change (i.e., $n_s = n_l$), and so

$$L/(T_0 C_p) = 2C_s\theta' \ln\left(1+\frac{\nu|\phi_s|^2}{n_l^2}\right) \approx 2\nu C_s\theta'\frac{|\phi_s|^2}{n_l^2}. \quad (45)$$

Equation (45) makes manifest that latent heat release is proportional to density change due to ordering of the liquid into solid.

The approach described in this subsection shows the correspondence of our formalism with model C type dynamics on long length scales, while incorporating new features in thermal transport that arise solely from the properties of the PFC model at the atomic scale (e.g., density re-arrangements,

defect flows, and other atomic-scale features attainable by the PFC density field).

To directly apply our modeling formalism to experiments, the basis of PFC temperature itself still requires more investigation. In the basic PFC model, temperature is buried implicitly in the r parameter. It is not clear how the θ function should relate it to the thermodynamic temperature T. Moreover, even with an appropriate θ function, due to the approximated form of the PFC free energy it is not clear if the model can reproduce the right physics across the extended phase space from vapour to solid. One solution is to restrict the investigation to a small part of phase space as has been done in the past. In what follows, we propose a new and quite different approach aimed at improving the thermodynamic consistency of PFC modeling, one that covers a wide range of a material's phase space.

V. TOWARDS A UNIFIED STRUCTURAL PFC MODEL WITH A PHYSICAL TEMPERATURE SCALE

Phase field crystal type models introduced to date have all contributed to making PFC models and their dynamics increasingly more consistent with thermodynamics. Two key features are, however, still lacking. The first deals with relating phenomenological PFC model parameters to thermodynamic temperature. For example, in the last section, we assumed that the parameter r in the original PFC model can be mapped to thermodynamic temperature through an unknown function $\theta(r)$, i.e., $T = T_0\theta(r)$. Several PFC models have presumed such relationships to interpret results in localized regions of model-specific phase diagrams with measurable quantities [11,34–36]. In this section, we go beyond previous approaches, and derive a general PFC-type formalism that explicitly relates model parameters to thermodynamic temperature, thus integrating naturally with the thermodensity formalism introduced in the previous sections. The second feature lacking in PFC modeling is a form for the free energy that is both tractable in its implementation and quantitative enough to incorporate phase changes over a robust range of density, temperature, and pressure space. Moreover, it is crucial to address this issue while allowing for the stabilization of complex crystalline structures, as well as for *efficient dynamical simulations* of phase transformations involving crystalline and disordered phases.

In the remainder of this section, we propose a new density functional formalism that addresses the above problems, leading to a PFC-style model that takes a significant step closer to a unified and quantitative PFC theory for pure materials.

A. Density functional approach: Expanding around the Van der Waals fluid

One of the key simplifications in PFC models is the expansion of the ideal [noninteracting] free energy. This approach makes the model analytically tractable and efficient to simulate. However, it severely limits the shape of the phase diagram, and also precludes a full solid-liquid-vapor description of a material's phase space. This is particularly felt near zero density, where the influence of the logarithm terms can lead to very low density phases (e.g., voids).

Here, we propose a model that starts with the full Van der Waals free energy to model long range (mean field) interactions in a system, complemented with multipoint correlations designed to capture short-range interactions and the emergence of solid phases. In particular, we break up the excess interaction energy of standard CDFT as a sum of a Van der Waals term and other excess effects, namely,

$$F[\rho, T] = F_{id}[\rho, T] + \Phi_{VdW}[\rho, T] + \Phi[\rho, T], \tag{46}$$

where

$$F_{id}[\rho, T] = \int d\mathbf{x}\, \rho k_B T(\ln(\lambda^3\rho) - 1) \tag{47}$$

and

$$\Phi_{VdW}[\rho, T] = -\int d\mathbf{x}\, k_B T\left\{\rho\ln(1-\tilde{b}\rho) + \frac{\tilde{a}}{k_B T}\rho^2\right\}. \tag{48}$$

The Van der Waals theory works well as its mean field limit is easy to analyze and can accurately describe disordered phases [37]. Note that we have named the Van der Waals parameters $\tilde{a}$ and $\tilde{b}$ in anticipation that these will be rescaled and renamed to a and b. The excess term $\Phi[\rho, T]$ is responsible for all short-range interactions not captured by $F_{id}[\rho, T] + F_{VdW}[\rho, T]$. By performing a functional expansion around a uniform reference density $\bar{\rho}$ corresponding to an equilibrium fluid phase, we arrive at the following the free energy,

$$\begin{aligned} F =& \bar{F}[\bar{\rho}, T] + \Phi[\bar{\rho}, T] + \int d\mathbf{x}\,(\bar{\mu} - V_{\text{ext}}(\mathbf{x}))\delta\rho(\mathbf{x}) \\ &+ \int d\mathbf{x} k_B T\left\{\rho\ln\left(\frac{\rho}{\bar{\rho}}\right) - \delta\rho + \rho\ln\left(\frac{1-\bar{\rho}\tilde{b}}{1-\rho\tilde{b}}\right)\right. \\ &\left. - \delta\rho\left(\frac{\bar{\rho}\tilde{b}}{1-\bar{\rho}\tilde{b}}\right) - \frac{\tilde{a}}{k_B T}\delta\rho^2\right\} \\ &- \frac{1}{2}\iint d\mathbf{x}\, d\mathbf{x}'\, k_B T\, \delta\rho(\mathbf{x})\tilde{C}^{(2)}(\mathbf{x}, \mathbf{x}', T)\delta\rho(\mathbf{x}') + \cdots, \end{aligned} \tag{49}$$

where $\delta\rho = \rho - \bar{\rho}$, V_{ext} is an external field, $\bar{\mu}$ is the chemical potential of the reference state, and

$$\begin{aligned} &\bar{F}[\bar{\rho}, T] \\ &= \int d\mathbf{x} k_B T\left\{\bar{\rho}\ln(\lambda^3\bar{\rho}) - \bar{\rho} - \bar{\rho}\ln(1-\tilde{b}\bar{\rho}) + \frac{\tilde{a}}{k_B T}\bar{\rho}^2\right\} \end{aligned} \tag{50}$$

is the free energy at the reference density. *At this stage*, we have identified by $\tilde{C}^{(2)}(\mathbf{x}, \mathbf{x}', T)$ as the general form of the direct two-point correlation function generated by the excess energy. We have denoted by three dots $[\cdots]$ the presence of higher order correlations which we have not written down as they are similarly generated by direct correlation functions. These will be assumed to act only on short wavelengths.

To proceed further, we introduce the reduced density, $n = (\rho - \bar{\rho})/\bar{\rho}$ or $\rho = \bar{\rho}(n+1)$, and the length scaling $\mathbf{r} = \mathbf{x}/R$, where R is a characteristic length scale, typically a lattice constant of one of the solid phases. In what follows, we will only consider the free energy difference relative to the reference state. Thus, we will work with $\Delta F = F - \bar{F}[\bar{\rho}, T] -$

$\Phi[\bar{\rho}, T]$. For completeness, we keep the terms linear in density, and define a rescaled chemical potential $\tilde{\mu} = \bar{\mu}/K_B T_0$ and external potential $\tilde{V}_{\text{ext}} = V_{\text{ext}}/k_B T_0$, where T_o is some reference temperature. While linear terms have an important role to play in the system pressure [38], they do not change the essence of the phase diagram. Combining the above elements gives a complete form of the proposed density functional,

$$\mathcal{F} = \int d\mathbf{r}\left[\tilde{\mu} - \tilde{V}_{\text{ext}} - \left(\frac{\tau}{1-b}\right)\right]n + \int d\mathbf{r}\,\tau\left\{(n+1)\ln\left(\frac{(n+1)(1-b)}{1-(n+1)b}\right) - \frac{a}{\tau}n^2\right\} - \frac{1}{2}\iint d\mathbf{r}\,d\mathbf{r}'\tau\, n(\mathbf{r})C^{(2)}(\mathbf{r},\mathbf{r}',\tau)n(\mathbf{r}') + \cdots, \quad (51)$$

where we have defined $\mathcal{F} = \Delta F/k_B T_0 \bar{\rho} R^d$, $b = \bar{\rho}\tilde{b}$, $a = \bar{\rho}^2\tilde{a}/k_B T_0$, the rescaled temperature $\tau = T/T_0$ and $C^{(2)} = \bar{\rho}R^d\tilde{C}^{(2)}$. The first and second lines in Eq. (51) contain effects from the ideal gas and the Van der Waals interactions, while the third line contains all the supplementary correlations required to stabilize solid phases.

Equation (51) is still incomplete as we are missing a form for the correlation function $C^{(2)}$ (and higher order terms in the $[\cdots]$) to create a full phase diagram. In practice, we want to affect short range ordering (e.g., solid phases) without affecting the long-wavelength behavior of the first two lines of Eq. (51). To proceed, we therefore separate the length scales of the ideal and Van der Walls terms (hereafter called "Van der Walls terms") from the supplemental correlation terms. Effectively, this amounts to enforcing the Van der Walls free energy terms only at long wavelengths by making them explicit functions of $n_{mf}(\mathbf{r}) \equiv \int d\mathbf{r}\chi(\mathbf{r}-\mathbf{r}')\mathbf{n}(\mathbf{r}')$, instead of the microscopically varying $n(\mathbf{r})$ field. This gives,

$$\mathcal{F} = \int d\mathbf{r}\left[\tilde{\mu} - \tilde{V}_{\text{ext}} - \left(\frac{\tau}{1-b}\right)\right]n_{mf} + \int d\mathbf{r}\,\tau\left\{(n_{mf}+1)\ln\left(\frac{(n_{mf}+1)(1-b)}{1-(n_{mf}+1)b}\right) - \frac{a}{\tau}n_{mf}^2\right\} - \frac{1}{2}\iint d\mathbf{r}\,d\mathbf{r}'\,\tau\, n(\mathbf{r})C^{(2)}(\mathbf{r},\mathbf{r}',\tau)n(\mathbf{r}') + \cdots. \quad (52)$$

Since the first line in Eq. (52) essentially maintains its mean field form, it will ensure that the long wavelength behavior of the model follows the correct Van der Walls thermodynamics. In proceeding as above, we have tacitly assumed that the short wavelength interactions removed from the original Van der Walls terms are subsumed into $C^{(2)}$ and the higher order correlation terms denoted by $[\cdots]$. This separation approach also avoids the severe constraint of requiring a positive density at the atomic scale. which forces the solid peaks to become very sharp in full CDFT calculations, and effectively kills the ability for *dynamical microstructure simulations, the quintessential advantage of PFC modelling*. In other words, the long wavelength behavior of the density in Eq. (52) will follow the correct Van der Walls thermodynamics, but the model still allows for smooth atomic-scale density oscillations that go both above and below the reference density, thus making it possible to model crystalline patterns in a computationally and analytically tractable manner.

We proceed next to simplify $C^{(2)}$ by breaking it into a structural term $C^{(2)}_{\text{struct}}$ that is used to stabilize crystalline states, and the other short-range correlations that now become subsumed into the $[\cdots]$ terms. Here, we employ an XPFC type kernel [39]. Namely, we define $C^{(2)}_{\text{struct}}$ as

$$C^{(2)}_{\text{struct}}(\mathbf{k}) = B_x e^{-T/T_0}\hat{C}_{\mathbf{k}} = B_x e^{-T/T_0} e^{-(\mathbf{k}-\mathbf{k}_0)^2/2\alpha^2}, \quad (53)$$

where B_x is a constant, k is the magnitude of $\mathbf{k}$ and k_o is the magnitude of $\mathbf{k}_0$, which defines the equilibrium reciprocal lattice vector of the first Bragg reflection of an 2D HCP lattice or a three-dimensional (3D) BCC lattice. The single peak XPFC formalism has the advantage of allowing for independent tuning of the lattice constant, elastic modulus or surface energetics due to the rapid decay of the correlation peak. Adding multiple Gaussian-type peaks such as those in Eq. (53) to $C^{(2)}_{\text{struct}}$ allows the model to describe different structures. Formally, there is one peak representing the main Bragg reflection peak from a set of crystal planes; in practice, only the first few [smallest] k-peaks are retained (e.g., one for 2D HCP and 3D BCC, two for 2D squares and 3D FCC, three for 3D HPC 3D [40], etc.). We can also expand to 3-point correlations following the recent work of Seymour *et al.* [41,42] and Alister *et al.* [43] to extend the range of crystalline structures to nonmetallic materials. It is noted that the use of higher order correlations typically requires that we go beyond 1-mode analysis of the free energy to retain the accuracy of simpler 1-mode approximations used for simpler structures. In this work, we will demonstrate the new model and its thermodensity coupling using a 1-peak $C^{(2)}_{\text{stuct}}$ function.

The original XPFC models parametrized temperature by $e^{-\sigma^2/\sigma_0^2}$, where σ is used as a phenomenological temperature parameter. Here, we follow the approach of Alster *et al.* [44] who effectively define $\sigma^2 \sim T/T_o$. This choice is more consistent with the temperature dependence of the Debye-Waller factor observed in experiments. The reference temperature T_0 here can in principle be different from the one used to scale the density functional expansion above. In this work, we aim to show that the model proposed in this section is physically consistent *and* robust enough to cover a wide range of material systems quantitatively. Thus, for convenience, we use the same reference temperature T_0 here as previously introduced to rescale the free energy functional.

The model described by to Eqs. (52)-(53) is still missing the higher order correlation terms separated out of the Van der Walls terms and buried in the $[\cdots]$ terms. In terms of a density expansion of the form $n = n_0 + \phi\sum_{\mathbf{G}} e^{i\mathbf{G}\cdot\mathbf{r}}$ the first two lines in Eq. (52) only give, to lowest order, average density (n_0) contributions. On the other hand, substituting Eq. (53) in the third line of Eq. (52) also gives a ϕ^2 amplitude contribution to the mean field of the theory, which only contributes to the free energy of the solid phase where $\phi > 0$. However, we still require a ϕ^4 theory to stabilize solid phases, and coupling terms between n_0 and ϕ to control the average density of the solidus. Another way to look at this is that we have enforced Van der Waals Theory (a complete theory), and crystallographic ordering at short wavelengths, but important thermodynamic contributions at short wavelengths are still missing.

To remedy this, we introduce a series of multipoint correlation functions that only affect the short wavelength behavior. These emerge from the $[\cdots]$ terms in Eq. (52). For this, we propose a set of correlations denoted $\zeta^{(m)}$, which are defined as products of two-point functions, given by

$$\zeta^{(m)} = \delta(\mathbf{r}_1 - \mathbf{r}_2)...\delta(\mathbf{r}_1 - \mathbf{r}_m) - \chi(\mathbf{r}_1 - \mathbf{r}_2)...\chi(\mathbf{r}_1 - \mathbf{r}_m), \tag{54}$$

where $\chi(k) = \exp(-k^2/(2\lambda^2))$ are long-wavelength kernels, defined in reciprocal space. (For simplicity, in this work we take the $\chi(\mathbf{r}_1 - \mathbf{r}_m)$ functions in Eq. (54) to be the same as the χ functions defined previously). In terms of the $\zeta^{(m)}$ functions, the final form of the model is written as

$$\begin{aligned}\mathcal{F} = &\int d\mathbf{r}\left[\tilde{\mu} - \tilde{V}_{\text{ext}} - \left(\frac{\tau}{1-b}\right)\right] n_{mf} \\ &+ \int d\mathbf{r}\,\tau\left\{(n_{mf}+1)\ln\left(\frac{(n_{mf}+1)(1-b)}{1-(n_{mf}+1)b}\right) - \frac{a}{\tau}n_{mf}^2\right\} \\ &- \frac{1}{2}B_x\int d\mathbf{r}\,\tau(\mathbf{r})\,e^{-\tau}n(\mathbf{r})\mathcal{F}^{-1}\left\{\int d\mathbf{k}'\hat{C}_{\mathbf{k}'}n(\mathbf{k}')\right\} \\ &+ \sum_{m=1}^{4}\frac{a_m}{m}\left(\int d\mathbf{r}_1..d\mathbf{r}_m\zeta^{(m)}(\mathbf{r}_1,..,\mathbf{r}_m)n(\mathbf{r}_1)..n(\mathbf{r}_m)\right),\end{aligned} \tag{55}$$

where $\mathcal{F}^{-1}$ represents the inverse Fourier transform. The last line in Eq. (55) comprises a series of correlation functions defined on short wavelengths, each weighted by dimensionless τ-dependent coefficients a_m. As an example, $\chi^{(2)}(\mathbf{k})$ contributes only at long wavelengths, thus acting as a low pass filter, but $\zeta^{(2)}(\mathbf{k}) = 1 - \chi^{(2)}(\mathbf{k})$ contributes at short wavelengths, thus essentially acting as high pass filter. The $\zeta^{(m)}$ correlation terms allow for control over the solid phase density-temperature properties in the phase diagram. The width of these short-range correlation functions also impacts the interface energy and solid compressibility. The $\hat{C}_{\mathbf{k}}(\mathbf{k})$ correlation function selects the crystal structure and also tunes the elastic modulus and interfacial energy. Long wavelength correlations are controlled by the Van der Walls theory. Figure 4 illustrates the shape of all 2-point kernels appearing in Eq. (55), in reciprocal space. The study of interface energies predicted by the model in Eq. (55) will be the topic of future work.

B. Equilibrium properties of the model

Mean field calculations of the model are done by using a 1-mode approximation approach. The long-wavelength correlation kernels χ and ζ are approximated as delta functions in $\mathbf{k}$ space. The phase diagram is computed by the usual common tangent or Maxwell equal area construction. To focus on demonstrating the salient features of the model in this work, we arbitrarily set $\tilde{\mu} = \tau/(1-b)$ and $V_{\text{ext}} = 0$, effectively canceling out all the linear terms. A resulting phase diagram is shown in Fig. 5. It features both a critical and a triple point, and a strongly asymmetric vapor/liquid phase separation as one expects from the Van der Waals theory. In addition, there are both liquid-solid and vapor-solid coexistence regions, which can be made quantitive by controlling the a, b, T_0, and a_m parameters. It is also noteworthy that the density axis for the uniform phases covers a physical range, starting at $n_o = -1$ (i.e., $\rho = 0$). The phase diagram also contains a solid phase, which has, for this choice of model parameters, a density ~25% higher than the liquid density near the triple point and approaches the liquid density at high temperature. To our knowledge this is the first PFC model describing solid-liquid-vapor phases over broad, and physically consistent, ranges in both temperature and density.

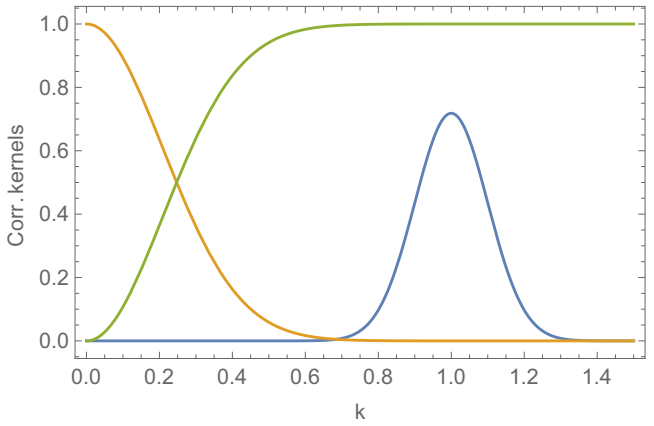

FIG. 4. Plot of the 2-point correlation kernels introduced in the model defined in Eq. (55), in reciprocal space. Blue: XPFC kernel (53), Orange: $\chi^{(2)}(\mathbf{k})$ smoothing kernel used to create the n_{mf} appearing in Eq. (55), Green: $\zeta^{(2)}(\mathbf{k})$ kernel modulating the short range correlation functions in Eq. (55). Parameter values used in plot: $B_x = 3.5$, $T/T_0 = 2.5$, $\alpha = 0.1$, $k_0 = 1$, $\lambda = 1$.

It is seen in Fig. 5 that using constant a_m factors rapidly reduces the solid-liquid density jump rapidly as temperature is increased. It possible to obtain a larger solid-liquid density jump and to decrease the divergence of the solid-liquid phase boundaries by introducing a temperature dependence in the a_m coefficients. To demonstrate this, we fit a_2 and a_3 with a second order polynomial in τ. We determine the parameters of the τ-expansion of a_2 and a_3 by interpolating between their

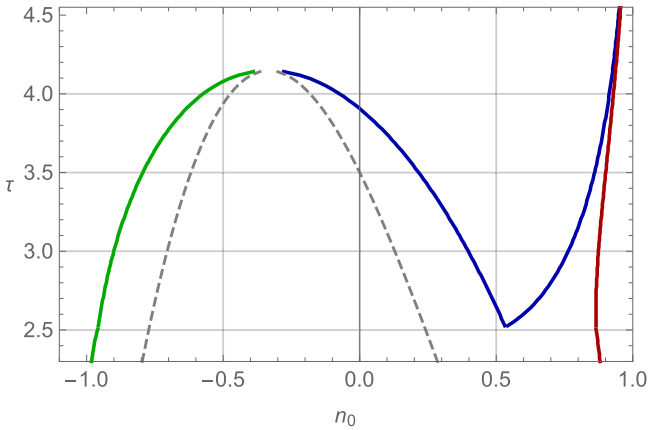

FIG. 5. Typical phase diagram of the model in Eq. (55). Green, blue and red are, respectively, the coexistence densities of vapor, liquid and periodic (solid) phases. Parameter values: $a = 7$, $b = 0.5$, $B_x = 3.5$, $a_2 = 5.45$, $a_3 = -2$, $a_4 = 0.1$.

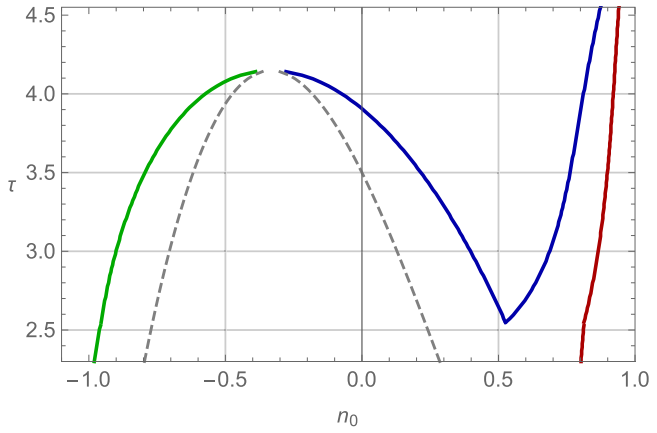

FIG. 6. Phase diagram of the the model in Eq. (55), with temperature dependent a_2 and a_3 coefficients in the short-range $\zeta^{(m)}$ correlation terms. Green, blue, and red are, respectively, the coexistence densities of vapor, liquid, and periodic phases. The dashed lines show the instability boundary of phases. The parameters are as in Fig. 5, except $a_2 = -2.26082 + 2.41018\tau + 0.06\tau^2$ and $a_3 = 0.689182 - 1.08982\tau + 0.06\tau^2$.

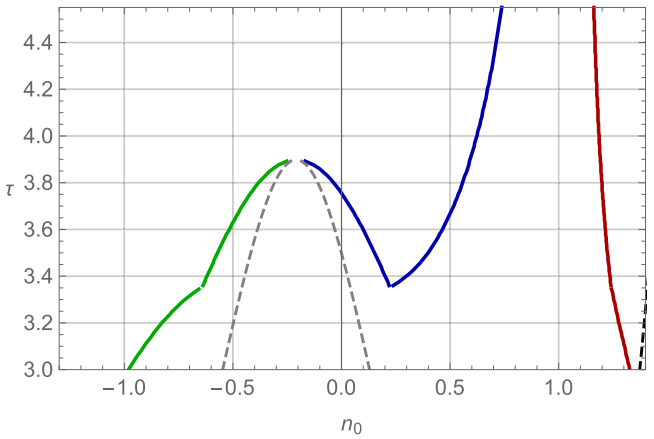

FIG. 7. Phase diagram of Eq. (55) with logarithm terms expanded to fourth order. Green, blue, and red are, respectively, the coexistence densities of vapor, liquid, and periodic phases. The dashed lines show the instability boundary of phases. Same parameter values as Fig. 5.

desired values at the lowest considered temperature τ_l (i.e., $a_{2,l}$, $a_{3,l}$) and highest considered temperature τ_h (i.e., $a_{2,h}$, $a_{3,h}$), while the prefactor Q of the quadratic term is fixed empirically for demonstration purposes. The specific form of the expansions for a_2 and a_3 used in this work are given by,

$$a_2(\tau) = Q\tau^2 - \frac{\left(-a_{2,h}+a_{2,l}+Q\tau_h^2-Q\tau_l^2\right)}{\tau_h-\tau_l}\,\tau - \frac{-a_{2,l}\tau_h + a_{2,h}\tau_l - Q\tau_h^2\tau_l + Q\tau_h\tau_l^2}{\tau_h-\tau_l},$$
$$a_3(\tau) = Q\tau^2 - \frac{\left(-a_{3,h}+a_{3,l}+Q\tau_h^2-Q\tau_l^2\right)}{\tau_h-\tau_l}\,\tau - \frac{-a_{3,l}\tau_h + a_{3,h}\tau_l - Q\tau_h^2\tau_l + Q\tau_h\tau_l^2}{\tau_h-\tau_l}. \quad (56)$$

A phase diagram with these τ-expanded correlation coefficients in the new PFC model is shown in Fig. 6, where the addition of this dependence has allowed us to widen the solid-liquid coexistence region. More careful fitting of τ_l and τ_h and their corresponding $a_{2,l}$, $a_{3,l}$, $a_{2,h}$, $a_{3,h}$ can expand the density jump further, but the form of the short-range correlations introduced cannot lead to completely parallel solid-liquid density lines, although not all materials have parallel solid-liquid coexistent lines.

The limitation in further expanding the solid-liquid density jump at high temperature arises due to the incompressibility of phases described by the Van der Waals formalism. In particular, the logarithm term in Eq. (55) diverges as the average density approaches $n^* = (1-b)/b$ (which corresponds to $n_0 = 1.5$ in the figures shown). This incompressibility limit is due to the excluded volume introduced in the Van der Waals theory, and is beneficial for modeling the uniform phases in the PFC model, but does not accommodate phases at arbitrarily higher density phases, namely the periodic (solid) phases.

C. Expansion of the Van der Walls terms

To model a larger range of solid-liquid density jumps in the proposed model, one can either relax the exclusion volume at higher density, or simply expand the uniform phase free energy. We proceed by expanding the logarithmic terms in Eq. (55), to recover a more flexible polynomial expansion of the free energy functional. The drawback of this approach is that the sharp cusp of the free energy at low density becomes less accurate. Higher order expansions or more elaborate fitting techniques such as a spline fitting could be applied to both accurately fit the sharp cusp at low density while simultaneously allowing a smooth description of liquid at high densities. These fitting techniques will not be studied here. Our aim here is to show how to create a complimentary version of the unified model that offers flexible control of the high density phases and their properties; the unified model of Eq. (55) can be used where the accuracy of the vapor phases is required.

We start by Taylor expanding the uniform part of the free energy in Eq. (55) to fourth order. The expansion is taken around $n_0 = 0.05$ to match the true free energy versus n_o of the full model as closely as possible across the temperature range we are interested in. Figure 7 shows the corresponding phase diagram. It features a wider liquid/solid density jump, but a significantly less asymmetric liquid and vapor coexistence. The parameters used are the same as those in Fig. 5.

To improve on the behavior of Fig. 7, we perform a tenth order Taylor expansion of the uniform free energy around $n_0 = 0.05$. Both vapor and liquid free energy wells are now more accurately captured, and this leads to a low-density part of the phase diagram very close to the one in Fig. 5, as shown in Fig. 8, although some discrepancy is still seen at lower temperatures due to the expanded nature of the uniform free energy. Note also that the solid-liquid density jump now becomes wider and more parallel at higher temperatures. To further expand the solid-liquid density jump, we can again assume a temperature dependance of a_2 and a_3 given by Eqs. (56). This leads to a wider and more parallel liquidus and solidus coexistence lines. A typical example is shown in

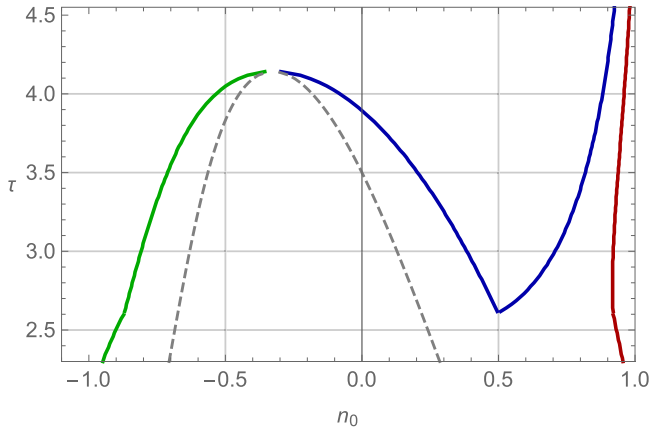

FIG. 8. Phase diagram corresponding to the system in Fig. 5, but with a tenth order expansion of the uniform free energy logarithm terms in Eq. (55). Notice the vapor-liquid phase separation starts to take a more asymmetric shape.

Fig. 9. Note that the slope of the liquid/solid coexistence line is smaller than the previous phase diagrams, demonstrating the model's flexibility.

Figure 10(a) shows the density-temperature-pressure phase diagram corresponding to the system in Fig. 9. The units of $[\mathcal{P}] = P/k_B\bar{\rho}T_oR^d$. The figure features solid-liquid, solid-vapor, and vapor-liquid coexistence regions, and is in excellent qualitative agreement with the expected phase diagram structure for pure materials. The corresponding pressure-temperature phase diagram [Fig. 10(b)] also shows experimentally expected behavior for pure substances. Along with the equilibrium phase boundaries, Fig. 10(b) also shows analytical estimates for the metastability regions of the different phases (dashed lines). Transforming from a metastable to stable phase requires a nucleation event. Crossing the metastable boundaries is associated in PFC with the appearance of an unstable wavelength.

In general, once the parameters setting the phase diagram characteristics of the uniform and crystal phases are

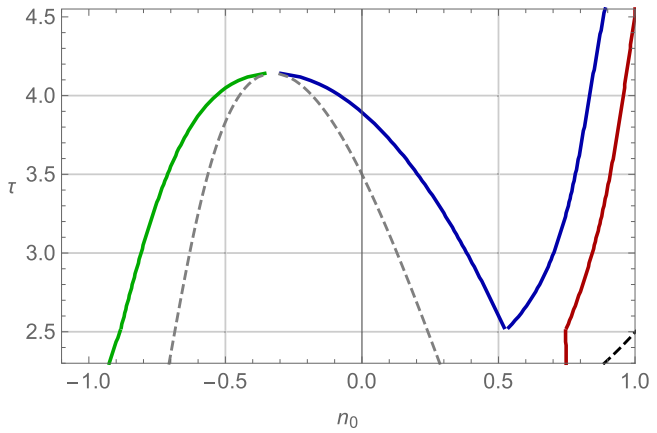

FIG. 9. Same system as in Fig. 8 but with a temperature dependance in the a_2 and a_3 coefficients. The density jump and slope of the liquid/solid coexistence lines are now more parallel and have smaller slopes. Here, $a_2 = -1.3825 + 1.66\tau + 0.05\tau^2$ and $a_3 = 0.572045 - 0.885455\tau + 0.05\tau^2$.

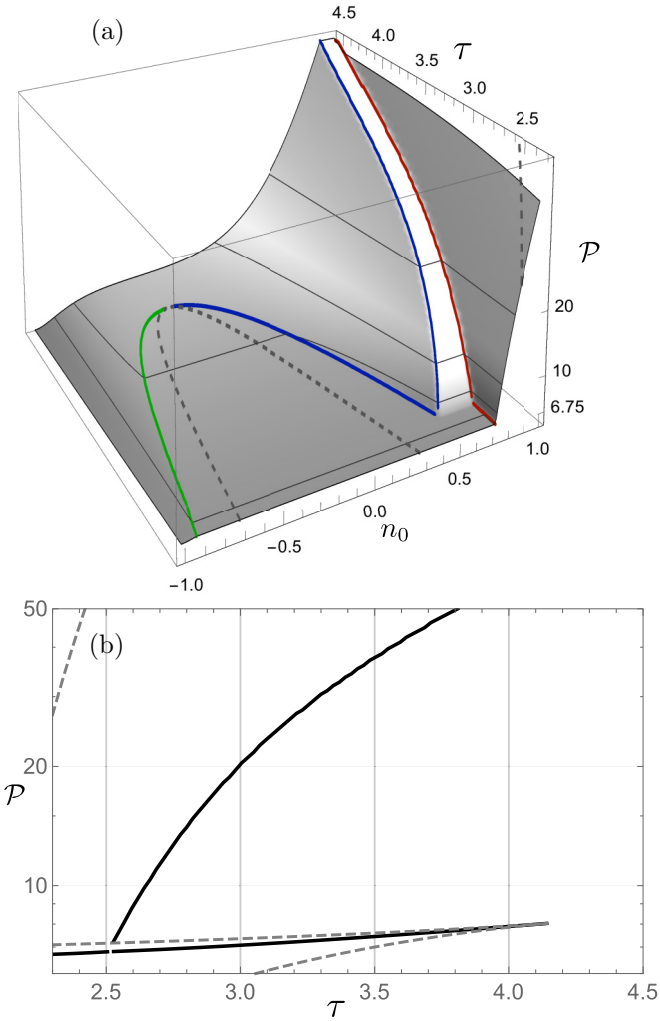

FIG. 10. (a) Reduced pressure-temperature-density phase diagram corresponding to the system in Fig. 9. The dashed lines show the instability boundary of phases. (b) Pressure-temperature phase diagram of the system in Fig. 9, featurig vapor, liquid, and solid phases as well as coexistence lines. Dashed lines are metastability lines.

determined, the other parameters of the model can then be sought to set the elastic modulus (solid), surface energies, compressibility, and so on. Using a fourth order expansion provides the barebones structure for a somewhat qualitatively correct phase diagram. The tenth order expansion provides a much more accurate description of the entire material system. Higher order expansions or different fitting techniques can be used to better match the vapor/liquid phase diagrams in the regions of interest. It is noteworthy that the use of the $\zeta^{(m)}$ correlation functions gives a new degree of control of the liquid/solid *and* solid state thermodynamics, without affecting the the selection of crystallographic symmetries or the vapor/liquid properties. Furthermore, making the coefficients of the $\zeta^{(m)}$ functions have temperature dependence can provide added flexibility to match both the slope and width of the liquid/solid coexistence in a wide range of materials.

The phase field crystal type of theory derived in this section, i.e., Eq. (55) and its variants that employ an expanded

form of the uniform phase free energy lead to an accurate description of three phase equilibrium in materials whose triple and critical points are not too far from one another in temperature. The proposed formalism makes it possible to model both critical point phenomena and very low density phases, solidification of crystalline phases from liquid or vapour, as well as the signature elastic/plastic phenomena in all PFC phenomenologies. These are important features for modeling solidification, CVD processes, and solidification shrinkage.

VI. COUPLING THE UNIFIED PFC MODEL TO THERMAL TRANSPORT

In this section, we return to the formalism of Sec. III B, and apply it to the unified model free energy derived in Sec. V. The main motivation for this is to apply the thermodensity coupling to a quantitative PFC type model that can be parameterized in (P, ρ, T) space. We re-write the free energy of Eq. (55), making explicit the temperature dependence of the coefficients a_m,

$$\mathcal{F} = \int d\mathbf{r}\left[\tilde{\mu} - \tilde{V}_{\text{ext}} - \left(\frac{\tau}{1-b}\right)\right] n_{mf} + \int d\mathbf{r}\,\tau\left\{(n_{mf}+1)\ln\left(\frac{(n_{mf}+1)(1-b)}{1-(n_{mf}+1)b}\right) - \frac{a}{\tau}n_{mf}^2\right\}$$
$$-\frac{1}{2}B_x\int d\mathbf{r}\,\tau(\mathbf{r})e^{-\tau}n(\mathbf{r})\mathcal{F}^{-1}\left\{\int d\mathbf{k}'\hat{C}_{\mathbf{k}'}n(\mathbf{k}')\right\} + \sum_{m=1}^{4}\frac{1}{m}\left(\int d\mathbf{r}_1,\ldots,d\mathbf{r}_m a_m(\tau)\zeta^{(m)}(\mathbf{r}_1,\ldots,\mathbf{r}_m)n(\mathbf{r}_1),\ldots,n(\mathbf{r}_m)\right).$$

We next calculate the rescaled internal energy $\tilde{e} = e/\bar{\rho}k_BT_0$, coarse grained on scales larger than the lattice constant, as was done in Sec. III using the smoothing function χ. This gives,

$$\tilde{e} = \chi * \left[f - \tau\frac{\delta\mathcal{F}}{\delta\tau}\right] = -an_{mf}^2 + \frac{1}{4}\sum_{m=2}^{4}\chi * \left\{\int d\mathbf{r}_2,\ldots,d\mathbf{r}_m[(a_m - \tau a_m')\zeta^m(\mathbf{r}_1,\ldots,\mathbf{r}_m)n(\mathbf{r}_1),\ldots,(\mathbf{r}_m)]\right\}. \quad (57)$$

Using the definition of the ζ^m functions and applying the delta functions within the ζ^m functions defined in Eq. (54), gives, after some manipulations and term collecting,

$$\tilde{e} = -an_{mf}^2 + \frac{1}{4}\sum_{m=2}^{4}(a_m - \tau a_m')\{\chi * [n^m] - (\chi * [n])^m\}. \quad (58)$$

We next take the time derivative of $\tilde{e}$, yielding

$$\frac{\partial\tilde{e}}{\partial t} = \frac{1}{4}\left\{\sum_{m=2}^{4}(-\tau a_m'')(\chi * [n^m] - (\chi * [n])^m)\right\}\frac{\partial\tau}{\partial t} + \frac{1}{4}\sum_{m=2}^{4}(a_m - \tau a_m')\frac{\partial}{\partial t}\{\chi * [n^m] - (\chi * [n])^m\} - a\frac{\partial}{\partial t}(\chi * [n])^2. \quad (59)$$

We next proceed as in Eq. (16) and substitute $\tilde{e}$ into the dimensionless energy transport equation,

$$\frac{\partial\tilde{e}}{\partial t} = \mathcal{C}^*\nabla^2\tau, \quad (60)$$

where $\mathcal{C}^* = K/\bar{\rho}R^2k_B$. Namely, substituting 59 for the left-hand side of Eq. (60) yields

$$\frac{1}{4}\left\{\sum_{m=2}^{4}(-\tau a_m'')(\chi * [n^m] - (\chi * [n])^m)\right\}\frac{\partial\tau}{\partial t} = \mathcal{C}^*\nabla^2\tau + a\frac{\partial}{\partial t}(\chi * [n])^2 - \frac{1}{4}\sum_{m=2}^{4}(a_m - \tau a_m')\frac{\partial}{\partial t}\{\chi * [n^m] - (\chi * [n])^m\}. \quad (61)$$

Equation (61) is the analog of Eq. (23) for the more general model of Eq. (55). Here, the source term and susceptibility factor pick up contributions from the moments of the PFC density field, highlighting the importance of atomic-scale variations of the PFC density on the thermal signature of microstructure evolution. The behavior of this model and its coupling to temperature will be studied in applications in rapid solidification in future publications.

VII. CONCLUSION

The first part of this work introduced a self-consistent formalism for coupling the dynamics of the PFC density to thermal transport. This makes it possible to model both atomic-scale structure changes and their effect on local heat release and diffusion during microstructure evolution. The formalism was first applied to the original PFC functional, showing the correspondence with model C type dynamics on long length scales, while on smaller length scales we demonstrated how density ordering at the atomic scale directly impacts the process of latent heat release and recalescence during early stage nucleation.

The second part of this work addressed two severe shortcomings of traditional PFC models, namely that they are too simplistic in their free energy construction and their temperature dependance/parameterization to describe the phase diagrams of pure materials quantitatively over a wide range of (P, ρ, T) space. Specifically, we developed a new PFC type model that decomposes the free energy of a pure material into a Van der Waals contribution that acts at long wavelengths and an excess contribution that controls short wavelength

interactions through the use of two classes of multipoint correlation functions, one of which includes the XPFC type correlation kernels used to control crystal structure, and the other of which controls the solid-liquid density jump and the solidus and liquidus slopes over a range of temperatures. This formalism unifies the description of uniform phases at low densities and over a wide range of temperatures and pressures with the description of high density solid phases with different crystallographies, the latter of which was the hallmark of previous XPFC models. Moreover, its smooth density profile allows for multiscale simulations and is analytically accessible.

The third part of this work applied the temperature-density coupling formalism discussed in the first part of the paper to the aforementioned unified PFC model. This leads to a thermal diffusion equation that, when combined with the usual Langevin dynamics of the PFC density field can be used to study thermodensity interactions crucial to processes in rapid crystallization, as well as in other phase transformations that occur in pure materials, over a wide range of their (P, ρ, T) phase space.

The unifying features of the new PFC model introduced in this work, and it use of a physical thermodynamic temperature and density scales makes it amenable to modeling the thermodynamic and elastic properties of pure materials quantitatively. One important future direction is to compare the properties of this new PFC model to those of a Lennard-Jones system [45,46]. Another future direction is the development of a quantitative binary alloy PFC model whose species densities ρ_A and ρ_B are independently described by Eq. (55) but are coupled through a suitably chosen A-B correlation function. Such an alloy model would be applicable to the study of numerous processes in rapid solidification, including recalescence, cavitation and void formation, thermal-stress-induced dislocations, and cell formation.

ACKNOWLEDGMENT

The authors would like thank the Natural Sciences and Engineering Research Council of Canada (NSERC) for funding.

[1] J. S. Langer, Instabilities and pattern formation in crystal growth, Rev. Mod. Phys. **52**, 1 (1980).
[2] J. A. Dantzig and M. Rappaz, *Solidification* (EPFL Press, Lausanne, Switzerland, 2009).
[3] E. O. Olakanmi *et al.*, A review on selective laser sintering/melting (SLS/SLM) of aluminium alloy powders: Processing, microstructure, and properties, Prog. Mater. Sci. **74**, 401 (2015).
[4] R. Acharya, J. A. Sharon, and A. Staroselsky, Prediction of microstructure in laser powder bed fusion process, Acta Mater. **124**, 360 (2017).
[5] V. D. Divya, R. Muñoz-Moreno, O. M. D. M. Messé, J. S. Barnard, S. Baker, T. Illston, and H. J. Stone, Microstructure of selective laser melted CM247LC nickel-based superalloy and its evolution through heat treatment, Mater. Charact. **114**, 62 (2016).
[6] J. H. Martin, B. D. Yahata, J. M. Hundley, J. A. Mayer, T. A. Schaedler, and T. M. Pollock, 3D printing of high-strength aluminium alloys, Nature **549**, 365 (2017).
[7] B. Echebarria, R. Folch, A. Karma, and M. Plapp, Quantitative phase-field model of alloy solidification, Phys. Rev. E **70**, 061604 (2004).
[8] M. Plapp, Unified derivation of phase-field models for alloy solidification from a grand-potential functional, Phys. Rev. E **84**, 031601 (2011).
[9] N. Provatas and K. Elder, *Front Matter*, pages I–XIII (Wiley-VCH Verlag GmbH & Co. KGaA, New York, 2010).
[10] T. V. Ramakrishnan and M. Yussouff, First-principles order-parameter theory of freezing, Phys. Rev. B **19**, 2775 (1979).
[11] K. R. Elder and M. Grant, Modeling elastic and plastic deformations in nonequilibrium processing using phase field crystals, Phys. Rev. E **70**, 051605 (2004).
[12] K. R. Elder, N. Provatas, J. Berry, P. Stefanovic, and M. Grant, Phase-field crystal modeling and classical density functional theory of freezing, Phys. Rev. B **75**, 064107 (2007).
[13] K.-A. Wu and A. Karma, Phase-field crystal modeling of equilibrium bcc-liquid interfaces, Phys. Rev. B **76**, 184107 (2007).
[14] S. Majaniemi and N. Provatas, Deriving surface-energy anisotropy for phenomenological phase-field models of solidification, Phys. Rev. E **79**, 011607 (2009).
[15] K.-A. Wu, M. Plapp, and P. W. Voorhees, Controlling crystal symmetries in phase-field crystal models, J. Phys.: Condens. Matter **22**, 364102 (2010).
[16] J. Berry and M. Grant, Modeling Multiple Time Scales During Glass Formation with Phase-Field Crystals, Phys. Rev. Lett. **106**, 175702 (2011).
[17] J. Berry, N. Provatas, J. Rottler, and C. W. Sinclair, Phase field crystal modeling as a unified atomistic approach to defect dynamics, Phys. Rev. B **89**, 214117 (2014).
[18] L. Gránásy, G. Tegze, G. I. Tóth, and T. Pusztai, Phase-field crystal modeling of crystal nucleation, heteroepitaxy and patterning, Philos. Mag. **91**, 123 (2011).
[19] H. Emmerich, H. Löwen, R. Wittkowski, T. Gruhn, G. I. Tóth, G. Tegze, and L. Gránásy, Phase-field-crystal models for condensed matter dynamics on atomic length and diffusive time scales: An overview, Adv. Phys. **61**, 665 (2012).
[20] V. Fallah, A. Korinek, N. Ofori-Opoku, N. Provatas, and S. Esmaeili, Atomistic investigation of clustering phenomenon in the AlCu system: Three-dimensional phase-field crystal simulation and HRTEM/HRSTEM characterization, Acta Mater. **61**, 6372 (2013).
[21] P. Jreidini, G. Kocher, and N. Provatas, Classical nucleation theory in the phase-field crystal model, Phys. Rev. E **97**, 042802 (2018).
[22] J. W. Elmer, S. M. Allen, and T. W. Eagar, Microstructural development during solidification of stainless steel alloys, Metall. Trans. A **20**, 2117 (1989).
[23] J. H. Lienhard IV and J. H. Lienhard V, *A Heat Transfer Textbook (Third ed.)* (Phlogiston Press, Cambridge, MA, 2008).
[24] G.-X. Wang, R. Goswami, S. Sampath, and V. Prasad, Understanding the heat transfer and solidification of plasma-sprayed yttria-partially stabilized zirconia coatings, Mater. Manuf. Processes **19**, 259 (2004).

[25] C. E. Wickersham, G. Bejor, and J. E. Green, Impulse stimulated "explosive" crystallization of sputter deposited amorphous (In,Ga)Sb films, Solid State Commun. **27**, 17 (1978).

[26] L. Nikolova, T. LaGrange, M. J. Stern, J. M. MacLeod, B. W. Reed, H. Ibrahim, G. H. Campbell, F. Rosei, and B. J. Siwick, Complex crystallization dynamics in amorphous germanium observed with dynamic transmission electron microscopy, Phys. Rev. B **87**, 064105 (2013).

[27] G. Kocher and N. Provatas, New Density Functional Approach for Solid-Liquid-Vapor Transitions in Pure Materials, Phys. Rev. Lett. **114**, 155501 (2015).

[28] U. Marini Bettolo Marconi and P. Tarazona, Dynamic density functional theory of fluids, J. Chem. Phys. **110**, 8032 (1999).

[29] The coefficients r, B_x and R are formally related to the coefficients $\hat{C}_n$ of the Fourier space expansion of $\bar{\rho}C(|\vec{x}-\vec{x}'|) = (-\bar{\rho}\hat{C}_0 - \bar{\rho}\hat{C}_2\nabla^2 - \bar{\rho}\hat{C}_4\nabla^4)\delta(\vec{x}-\vec{x}')$, which are evaluated at some reference density and reference temperature $(\bar{\rho}, T_0)$ on the liquidus of the phase diagram. In the PFC literature, it is tacitly assumed that as one moves away form $(\bar{\rho}, T_0)$ in temperature, these coefficients can vary with temperature in some sensible way. It is in this way that r is typically assigned the role of PFC temperature; B_x and R are typically considered to be constant.

[30] K. R. Elder, M. Katakowski, M. Haataja, and M. Grant, Modeling Elasticity in Crystal Growth, Phys. Rev. Lett. **88**, 245701 (2002).

[31] G. Kocher, N. Ofori-Opoku, and N. Provatas, Incorporating Noise Quantitatively in the Phase Field Crystal Model Via Capillary Fluctuation Theory, Phys. Rev. Lett. **117**, 220601 (2016).

[32] P. C. Hohenberg and B. I. Halperin, Theory of dynamic critical phenomena, Rev. Mod. Phys. **49**, 435 (1977).

[33] K. R. Elder, M. Grant, N. Provatas, and J. M. Kosterlitz, Sharp interface limits of phase-field models, Phys. Rev. E **64**, 021604 (2001).

[34] A. Jaatinen, C. V. Achim, K. R. Elder, and T. Ala-Nissila, Thermodynamics of bcc metals in phase-field-crystal models, Phys. Rev. E **80**, 031602 (2009).

[35] A. Adland, A. Karma, R. Spatschek, D. Buta, and M. Asta, Phase-field-crystal study of grain boundary premelting and shearing in bcc iron, Phys. Rev. B **87**, 024110 (2013).

[36] E. Asadi and M. A. Zaeem, Quantifying a two-mode phase-field crystal model for bcc metals at melting point, Comput. Mater. Sci. **105**, 101 (2015).

[37] M. Plischke and B. Bergersen, *Equilibrium Statistical Physics*, 3rd ed. (World Scientific, Singapore, 2006).

[38] Z.-L. Wang, Z.-F. Huang, and Z. Liu, Elastic constants of stressed and unstressed materials in the phase-field crystal model, Phys. Rev. B **97**, 144112 (2018).

[39] M. Greenwood, N. Provatas, and J. Rottler, Free Energy Functionals for Efficient Phase Field Crystal Modeling of Structural Phase Transformations, Phys. Rev. Lett. **105**, 045702 (2010).

[40] M. Greenwood, J. Rottler, and N. Provatas, Phase-field-crystal methodology for modeling of structural transformations, Phys. Rev. E **83**, 031601 (2011).

[41] M. Seymour and N. Provatas, Structural phase field crystal approach for modeling graphene and other two-dimensional structures, Phys. Rev. B **93**, 035447 (2016).

[42] M. Seymour, Study of Multi-Point Interactions in PFC Models for Complex Structural Transformations, Ph.D. Thesis, McGill University, 2017.

[43] E. Alster, D. Montiel, K. Thornton, and P. W. Voorhees, Simulating complex crystal structures using the phase-field crystal model, Phys. Rev. Mat. **1**, 060801(R) (2017).

[44] E. Alster, K. R. Elder, J. J. Hoyt, and P. W. Voorhees, Phase-field-crystal model for ordered crystals, Phys. Rev. E **95**, 022105 (2017).

[45] L. Mederos, G. Navascues, P. Tarazona, and E. Chacon, Perturbation weighted-density approximation: The phase diagram of a lennard-jones system, Phys. Rev. E **47**, 4284 (1993).

[46] D. D. Carley, Theoretical thermodynamic functions for a lennard-jones system in the liquid and vapur region, J. Chem. Phys. **69**, 4291 (1978).